



Fabrication of robust nanostructured (Zr)BiVO₄/nickel hexacyanoferrate core/shell photoanodes for solar water splitting

Maged N. Shaddad^{a,*}, Prabhakarn Arunachalam^a, Joselito Labis^b, Mahmoud Hezam^{b,*}, Abdullah M. Al-Mayouf^{a,*}

^a *Electrochemical Sciences Research Chair, Department of Chemistry, Science College, King Saud University, Riyadh, Saudi Arabia*

^b *King Abdullah Institute for Nanotechnology, King Saud University, Riyadh, Saudi Arabia*



ARTICLE INFO

Keywords:

Solar water splitting
Oxygen evolution catalyst
Bismuth vanadate
Prussian blue

ABSTRACT

BiVO₄ is one of the most promising semiconductors for photoelectrochemical water splitting. BiVO₄ is, however, limited by poor charge separation and slow oxygen evolution dynamics, for which surface modification with oxygen evolution catalysts (OECs) becomes indispensable. Among many OECs, Prussian blue type coordination polymers have lately attracted an escalating research interest attributable to their low cost, chemical robustness and easy synthesis using nontoxic earth-abundant elements. In this study, we report a simple method for efficient surface modification of Zr-doped BiVO₄ nanostructured electrodes with an amorphous Ni-Fe based Prussian blue (NiFePB) polymer. The method resulted in a remarkable 10-fold enhancement of photocurrent (3.23 mA cm⁻² at 1.23 V versus the reversible hydrogen electrode RHE) and a low onset potential of 0.208 V versus RHE, which are both records for Prussian blue (PB) type materials. Our coating method results in a (Zr)BiVO₄/NiFePB core-shell structure, in which a 10–15 nm NiFePB shell makes a superior conformal coating with complete coverage on the (Zr)BiVO₄ nanoparticles. The high conformity and amorphous nature of the coating are believed to be key features for the high photocatalytic activity and for a high photocorrosion resistance of the photoanodes during > 50 h of AM1.5 G solar illumination. Our method illustrates the large potential of Prussian blue type materials, when properly coated, as efficient and highly stable OECs.

1. Introduction

The generation of solar fuels (i.e., transforming solar energy into chemical energy stored in molecular bonds of generated compounds) stands, in principle, as a feasible choice to secure a substantial share of our global energy demands using clean energy resources [1,2]. In this regard, solar water splitting using photoelectrochemical (PEC) devices is one of the promising technologies for efficient and low-cost production of hydrogen, the cleanest solar fuel [2,3]. In a PEC cell, a semiconductor material presumably capable of absorbing the major portion of the solar spectrum is used to perform the fundamental step of harvesting the solar radiation. The conduction and valence band edges of the semiconductor must lie respectively above (i.e., more positive to) the O₂/H₂O oxidation potential, and below the H⁺/H₂ reduction potential. Before reaching the oxidation/reduction sites, both electrons and holes need to travel through the semiconductor, necessitating efficient transport properties for both carriers. Several semiconductor oxide photoelectrodes (e.g., TiO₂ [4,5], Fe₂O₃ [6,7], WO₃ [8,9], CdS [10,11], BiVO₄ [12,13], etc.) have been used for the fabrication of PEC

water splitting devices. Among these, BiVO₄ combines a relatively narrow band gap of ~ 2.4–2.5 eV, good energy alignment with oxidation/reduction potentials, cheap and nontoxic earth-abundant ingredients, and a rational, as well as progressively improving, stability. However, BiVO₄ presents its own shortcomings of poor charge transport properties, slow oxygen evolution, and fast bulk and surface electron-hole recombination [12,13]. The poor transport drawback is customarily addressed by using back-illumination during the artificial photosynthesis process [14,15], reducing the distance to be travelled by electrons, which have diffusion lengths reported between 10–100 nm [16,17]. Further, doping with transition metal cations, replacing the V⁵⁺ sites, has been a greatly successful strategy in improving the e-h separation efficiency and increasing electron mobility in this n-type material [13,16,17]. We recently showed that replacing the Bi³⁺ sites using Zr⁴⁺ can also lead to similar improvements [18,19]. Nanstructuring of the fabricated electrodes, which increases the depletion layer width and reduces the distance to be travelled by the minority carriers as well, has been another successful approach to enhance the photocatalytic activity [12,15,17,20]. The slow oxygen evolution can

* Corresponding authors.

E-mail addresses: mshaddad@ksu.edu.sa (M.N. Shaddad), mhezam@ksu.edu.sa (M. Hezam), amayouf@ksu.edu.sa (A.M. Al-Mayouf).

be improved by loading oxygen evolution catalysts (OECs) such as IrO_x [12,21], CoPi [22–24], FeOOH [25–27], and NiOOH [27,28] on the BiVO₄ surface. OECs provide sites for efficient hole collection by the water molecules in addition to possibly passivating the BiVO₄ surface against e–h surface recombination. They also provide a protection layer for the BiVO₄ surface against photocorrosion, which primarily takes place by the dissolution of V⁵⁺ ions from the BiVO₄ lattice during the water oxidation process [29].

Indeed, as the PEC performance of BiVO₄-based electrodes has been steadily progressing [12,13,30,31], the photostability of BiVO₄ photoanodes against photocorrosion becomes the main concern [29,32,33]. Different approaches have been developed in order to increase the lifetime of BiVO₄ photoelectrodes, e.g., deposition of an inert layer [33], using electrolytes with high concentration of V⁵⁺ ions [29], and deposition of layers of OECs [21–28]. The use of OECs, besides adding a spatial protection between BiVO₄ and the electrolyte, increases the rate of interfacial charge transfer. Having an interfacial charge transfer rate faster than the rate of photocorrosion is another key advantage of OECs in kinetically suppressing the photocorrosion effect [29].

An ideal OEC has to be water resistant, photostable, and maintain proper energy alignments with BiVO₄ and the electrolyte solution in use. Among many well studied OEC materials in the literature, Prussian blue (PB) type coordination polymers are low-cost, nontoxic, highly stable (only in neutral and acidic media) and easily synthesized materials that have recently been “diffidently ascending the stage” [34–41]. The PB type structure has the general formula: A_{2x}M_(3-x)[M'(CN)₆]₂·nH₂O, where M and M' are two metals, and A is an alkali ion [35]. A schematic drawing of PB type structure is shown in **Scheme 1**. Typically, the structure consists of two (similar or different) metal ions, each connected through cyanide bonds in an FCC structure. One metal ion is connected to the N side of the bond while the other is connected to the C side. The strong cyanide bonds between the metal ions render the cyanide-containing compound nontoxic and offer superior stability and reproducible responses of the material. At the same time, they result in a largely open framework that brings about several other advantages such as faster dynamics and mitigated charging effects. Alkali cations, e.g., K⁺, Na⁺, and water molecules, can intercalate into the large interstitial voids between the dications. When PB materials are used for photocatalysis, it is at those voids that water

oxidation is supposed to take place. In fact, it is not only the cyanide bonds that make the large voids; nonstoichiometry between the two dications, which is naturally the case in PB type materials, additionally allows for other voids in the PB framework [35,41,42].

The use of PB type coordination polymers in solar-based water splitting applications have been scarce, yet have taken many forms. We refer first to the work of Galán-Mascarós et al. (2013–2015), who had the lead in studying several metal hexacyanometalates as water oxidation catalysts [34–36]. Yamada et al. reported photoelectrochemical water oxidation catalyzed by a Pt-Co based PB complex [37]. Recently, Aksoy et al. reported water oxidation electro-catalyzed by an amorphous Co-Fe PB compound with an appreciable current density of 1 mA/cm² only at 510 mV [38]. Bui et al performed an overall water splitting system using two different PB polymers for the oxygen and hydrogen evolution reactions [39]. These reports have clearly demonstrated the potential of PB type materials in water oxidation catalysis and the strong need to pursue further investigations on cyanide-based compounds. A new strategy has been to couple the strong catalytic water oxidation activity of PB type materials, considering their low absorption in the UV-vis range, as OECs with other semiconductors that better absorb in the UV-vis region. In this direction, Shirakawa et al. used K₂[CdFe(CN)₆]-modified metal sulfide electrodes as H₂-evolving catalysts, where Fe(CN)₆^{3-/-4} redox mediators were simultaneously used as efficient scavengers of photogenerated holes [40]. Very recently, Hegner et al. reported fairly stable BiVO₄ water oxidation photoanodes decorated with a CoFe-based PB material that exhibit a current density of ~1 mA/cm² at 1.23 V vs. RHE and a noticeably low overpotential of 0.3 V [41]. In this work, we report a new and simple method for the surface modification of Zr-doped BiVO₄ with a Ni-Fe PB (NiFePB) polymer that resulted in an extraordinary 10-fold enhancement of the photocurrent (3.23 mA/cm² at 1.23 V vs. RHE) and a remarkably low onset potential of 0.208 V, which are, to our knowledge, two pioneering records for PB type materials. Moreover, the resulting electrodes showed a superior photostability with no current loss over more than 50 h of AM1.5 G solar illumination.

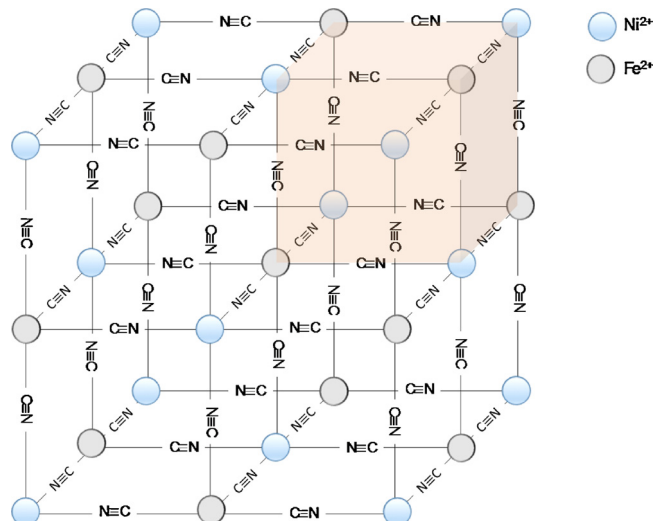
2. Experimental

2.1. Fabrication of electrodes

Zr-doped BiVO₄ photoanodes were prepared according to a previous optimization process [18], which involves Bi electrodeposition on FTO-coated glass, with Zr added as 2.5 mol.% of ZrOCl₂·8H₂O to the Bi³⁺ plating bath, followed by a reaction with vanadyl acetylacetone VO(acac)₂. The NiFePB polymer is coated on the (Zr)BiVO₄ electrodes using a two-step process. First, metallic nickel is electrodeposited from a 0.02 M NiCl₂ solution in DMSO. The electrodeposition was performed at -2.0 V vs. Ag/AgCl, and an optimization process of this step was performed through varying the total deposition charge from 10 to 50 mC/cm². The optimized charge density (for best delivered photocurrent from the PEC device) was found to be 30 mC/cm² (Figure S10). After Ni electrodeposition, the fabricated photoanodes were rinsed with MilliQ water and then dipped in 0.02 M K₃[Fe(CN)₆] solution at 25 °C without stirring. This step was also optimized by using different dipping times (1–30 min) with the highest photocurrent found at 20 min (Figure S11). The synthetic processes of the photoanodes are schematically shown in **Scheme S1**.

2.2. Materials characterization

Optimized electrodes, i.e., bare BiVO₄ and (Zr)BiVO₄ decorated with NiFePB coating using Ni charge density of 30 mC/cm² and 20 min dipping time in the K₃[Fe(CN)₆] solution, were characterized for their morphology and composition by field emission scanning electron microscopy (FE-SEM) (JEOL, JSM-7000 F) equipped with an INCA 400 Oxford EDS analyzer and by a high-resolution transmission electron



Scheme 1. Schematic of a unit cell of the FCC structure of Ni²⁺Fe²⁺(CN)₆ Prussian blue catalyst (abbreviated in the text as NiFePB). The Ni and Fe cations are bridged by the strong cyanide bonds. Alkali cations, e.g. K⁺, can intercalate in the interstitial sites at the middle of each of the eight subcells (one of them is orange-colored). Under full occupancy of the interstitials by K⁺ ions, the material is reduced to K₂Ni²⁺Fe²⁺(CN)₆. Zeolitic water can however occupy some of the sites during the dynamic process of catalytic water oxidation.

microscope (HR-TEM) (JEOL, JEM-2100 JEOL) operating at 200 kV. The structure of the optimized films was studied by X-ray diffraction (XRD) using a Rigaku Miniflex 600 X-ray diffraction system with copper K α radiation ($\lambda = 1.5418 \text{ \AA}$) and a scan speed of 3° min^{-1} . Surface analysis was carried out by X-ray photoelectron spectroscopy (XPS) (JEOL, JPS-9200). The optical properties were determined using an ultraviolet-visible (UV-vis) spectrophotometer (Shimadzu, UV-2600). Fourier transform infrared absorption spectroscopy (FT-IR) was recorded using a Bruker Tensor 27 FT-IR spectrometer.

2.3. Photoelectrochemical measurements

PEC characterization of the prepared electrodes was carried out by cyclic voltammetry in a 0.1 M phosphate buffer solution (PBS) of pH 7.5. Alternatively, 0.5 M H₂O₂ (30%) was added to the electrolyte as a hole scavenger in order to determine the charge transfer and charge separation efficiencies. The electrochemical cell was composed of the working electrode, an Ag/AgCl (3 M KCl) reference electrode and a Pt wire as a counter electrode. All potentials were referred to the reversible hydrogen electrode (RHE). All PEC measurements were performed using an AutoLab potentiostat (PGSTAT30). Measurements were carried out both in the dark and under simulated sunlight illumination. Sunlight was simulated using a 300 W Xe lamp with an AM1.5 G solar filter resulting in 100 mW/cm^2 output power (1 sun). A photocurrent spectroscopy system (Instytut Fotonowy) having a 150 W xenon lamp and a monochromator was used for the incident photon to current conversion efficiency (IPCE) measurements with the photocurrent measured at 1.23 V vs. RHE at 10 nm spectral steps. Calculation details of IPCE, light harvesting efficiency (LHE), charge transfer efficiency (η_{ct}), and charge separation efficiency (η_{cs}) can be found in the Supplementary Information. PEC oxygen evolution was monitored by an oxygen analyzer (Oxysense 325i). The tested cells were placed in a sealed compartment, and the electrolyte solution was first bubbled with argon for $\sim 1 \text{ h}$ prior to the experiments.

3. Results

3.1. Structural and morphological studies

Fig. 1(a–c) shows the FE-SEM images of the best optimized films at different preparation stages: (Zr)BiVO₄ photoanodes before Ni electrodeposition (Fig. 1a), after Ni electrodeposition (Fig. 1b), and after dipping into the potassium ferricyanide solution (Fig. 1c). The three images confirm an extremely homogeneous coverage of both Ni and, subsequently, NiFePB on the (Zr)BiVO₄ surface (see also Figures S1–S3 for EDS areal elemental maps). This homogeneity is further locally investigated by the FE-TEM images shown in Fig. 1(d–e). As seen in

Fig. 1(d–e), our two-step method results in an astonishingly conformal coverage of NiFePB on the (Zr)BiVO₄ nanoparticle surfaces, taking the form of a thin shell of $\sim 10\text{--}15 \text{ nm}$ thickness. Fig. 1e shows a high resolution TEM (HRTEM) image of one (Zr)BiVO₄/NiFePB core-shell nanoparticle. No lattice fringes are observed in the NiFePB shell, implying an amorphous NiFePB structure. As will be discussed below, the conformal coverage and amorphous structure are key features, respectively, for long-term stability and high efficiency of PB type catalysts. The EDS spectrum in Fig. 1f further confirms the existence of all elements in the (Zr)BiVO₄/NiFePB core-shell nanoparticles.

Fig. 2a shows the XRD measurements on the (Zr)BiVO₄ films before and after NiFePB deposition. All diffractions are indexed to monoclinic BiVO₄ (m-BiVO₄, JCPDS 83–1698) [18], with the absence of NiFePB diffraction peaks in the XRD pattern of the NiFePB decorated (Zr)BiVO₄ photoanode confirming the amorphous nature of the NiFePB coating.

XPS analysis was performed to study the surface of prepared films before and after NiFePB deposition as well as the valence state of the bound elements in the NiFePB polymer. As seen in the survey XPS spectra for the samples before and after NiFePB deposition (Figure S7), NiFePB deposition resulted in an evident cessation of the Bi, Zr and V XPS signals and the emergence of the N, Fe, Ni and K signals. As XPS is a highly surface sensitive technique, with an analysis depth of $\sim 10 \text{ nm}$, this result unambiguously confirms a uniquely conformal coating of NiFePB on the (Zr)BiVO₄ electrodes. Fig. 2(b–e) shows the high resolution XPS spectra for the C 1 s, N 1 s, Fe 2p and Ni 2p regions for the NiFePB deposited sample. The C 1 s peak is centered at $\sim 285 \text{ eV}$ and can be deconvoluted into two peaks: a C–C (sp^3) peak centered at 284.7 eV attributed to adventitious carbon contaminants, and a wider peak centered at 285.1 eV attributed to the C(sp)-N bond of the NiFePB polymer [43–45]. The N 1 s region shows a single peak centered at a binding energy of 397.7 eV, which is a well-known characteristic of the C–N bond [39,46]. The locations of Fe 2p_{3/2} (707.5 eV) and Fe 2p_{1/2} (720.2 eV) indicate the existence of the Fe²⁺ state in this cyanide bridging compound [46,47]. Similarly, Ni 2p_{3/2} and Ni 2p_{1/2} peaks located at 855.8 and 874.5 eV, along with two satellite bands, indicate that Ni is in the Ni²⁺ oxidation state [39,45].

FT-IR measurements confirm our conclusions on the oxidation states of Fe and Ni in the NiFePB coating. Fig. 2f shows the FT-IR spectra of the films before and after NiFePB deposition. The spectra evidently reveal the distinctive C–N stretching mode at a frequency of $\sim 2095 \text{ cm}^{-1}$, which, according to the comprehensive study of Goberna-Ferron et al. [35], corresponds to the Fe²⁺–CN–Ni²⁺ band.

The absorption spectra of bare BiVO₄, (Zr)BiVO₄ and (Zr)BiVO₄/NiFePB core-shell photoanodes are shown in Figure S9. (Zr)BiVO₄/NiFePB photoanodes show considerably stronger light absorption than (Zr)BiVO₄ photoanodes with a relatively smaller bandgap. The bandgaps estimated from the onset of the absorption edges using Tauc plots

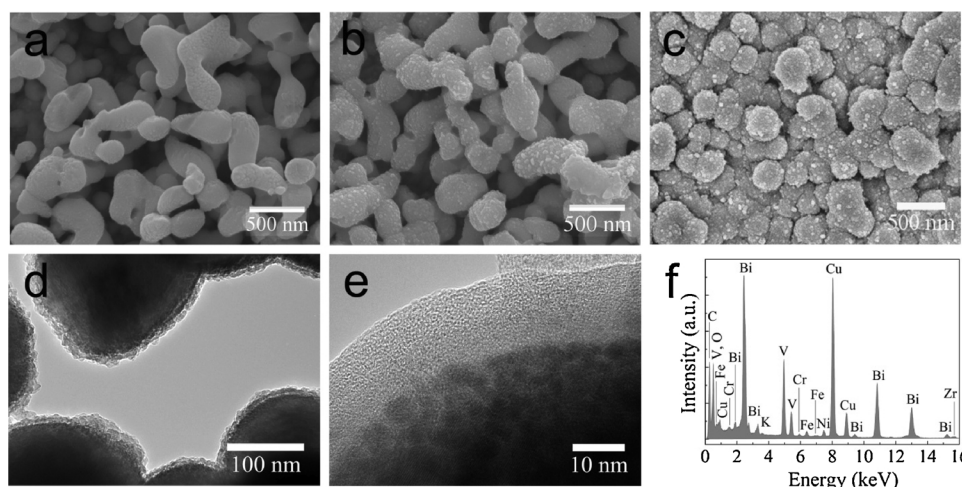


Fig. 1. (a–c) FE-SEM images of the (Zr)BiVO₄ photoanodes at different preparation stages: (a) before Ni electrodeposition (b) after Ni electrodeposition (c) after dipping into the Potassium ferricyanide solution. (d) TEM image of the resulting (Zr)BiVO₄ core/NiFePB shell structured nanoparticles. The complete coverage and superior uniformity of the NiFePB shell can be clearly observed. (e) High resolution TEM (HRTEM) image of one (Zr)BiVO₄ core/NiFePB shell nanoparticle. Unlike the core region, no lattice fringes are observed in the shell region confirming the amorphous nature of the NiFePB deposited shell. (f) EDS spectrum of the (Zr)BiVO₄/NiFePB core-shell electrode.

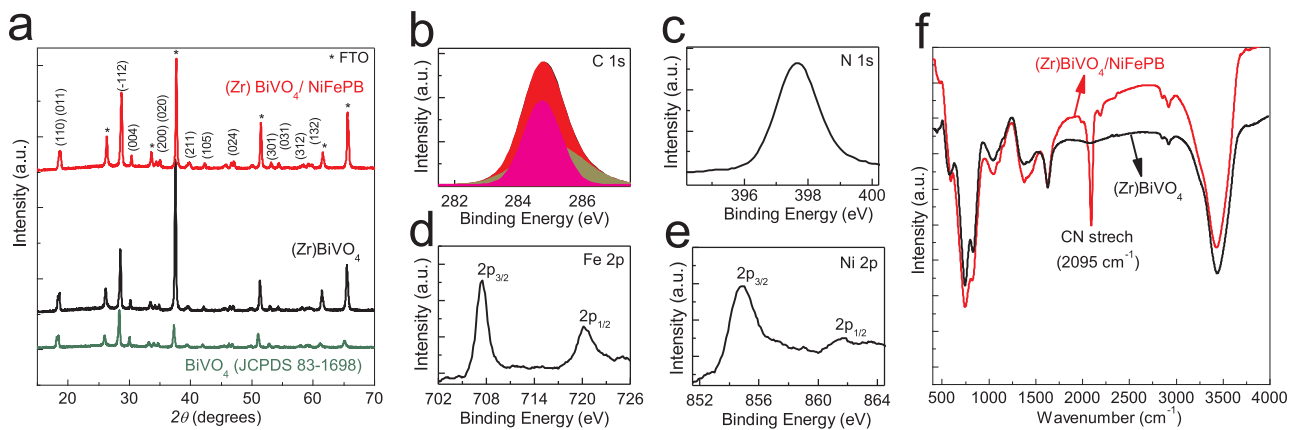


Fig. 2. (a) XRD patterns of a bare BiVO_4 electrode, $(\text{Zr})\text{BiVO}_4$ electrode and NiFePB deposited $(\text{Zr})\text{BiVO}_4$ electrode. No diffraction peaks of NiFePB polymer are observed. (b–e) High resolution XPS spectra of C 1 s, N 1 s, Fe 2p and Ni 2p regions, respectively, for the NiFePB decorated $(\text{Zr})\text{BiVO}_4$ electrode. (f) FT-IR spectra of the $(\text{Zr})\text{BiVO}_4$ electrode before (black) and after (red) NiFePB deposition. The C–N stretch band at 2095 cm^{-1} can be noticeably observed.

are found to be 2.47 eV and 2.43 eV for $(\text{Zr})\text{BiVO}_4$ and $(\text{Zr})\text{BiVO}_4$ –NiFePB photoanodes, respectively. The relatively lower bandgap energy noticed for NiFePB decorated film can be possibly attributed to interaction of the PB solid structure with BiVO_4 .

3.2. Photocatalytic activity

Fig. 3 shows the J–V curves for the best optimized $(\text{Zr})\text{BiVO}_4$ and $(\text{Zr})\text{BiVO}_4$ –NiFePB photoanodes under constant (Fig. 3a) and chopped (Fig. 3b) illumination of $100\text{ mW}\cdot\text{cm}^{-2}$. For the optimized $(\text{Zr})\text{BiVO}_4$ –NiFePB electrode, a ten-fold enhancement of the water oxidation photocurrent is achieved (3.23 mAcm^{-2} at $1.23\text{ V}_{\text{RHE}}$) compared to the corresponding $(\text{Zr})\text{BiVO}_4$ system. This substantial photocurrent enhancement is supplemented by a significant cathodic shift of the onset potential down to 208 mV . Both photocurrent and onset potential values are, to the best of our knowledge, records for Prussian blue type polymers in water oxidation PECs whether used as the main water splitting material or as OECs. For comparison, an electrode with only NiFePB coated directly on FTO with the same optimized conditions was prepared, and the J–V curves for the NiFePB/FTO and bare FTO are presented in Figure S13, showing no optical activity of the NiFePB coating alone.

J–V curves were also measured in the presence of H_2O_2 , an efficient hole scavenger for which the charge collection efficiency can be considered to be unity. This is supported by the well-reported literature on the easy oxidation of H_2O_2 by many oxidation catalysts, including BiVO_4 , even at very low onset potentials [48–52]. This examination will

help us investigate the efficiency of the NiFePB coating and consequently estimate the charge separation/collection efficiencies, as further detailed in the Supplementary Information. As seen in Fig. 3a, in the presence of H_2O_2 , the J–V curves of $(\text{Zr})\text{BiVO}_4$ show, as expected, a remarkable improvement in both onset potential (0.145 V) and photocurrent density ($\sim 3.2\text{ mAcm}^{-2}$ at $1.23\text{ V}_{\text{RHE}}$). Interestingly, these values closely match the PEC performance of our optimized electrode. Similar conclusions can be obtained from the IPCE measurements presented in Fig. 3c. A high IPCE of $\sim 50\%$ is obtained for the optimized $(\text{Zr})\text{BiVO}_4$ –NiFePB electrode above the band edge at $\sim 460\text{ nm}$, which is a nearly five-fold enhancement compared to the $(\text{Zr})\text{BiVO}_4$ values. On the other hand, IPCE measurements of $(\text{Zr})\text{BiVO}_4$ in the presence of a hole scavenger ($0.5\text{ M H}_2\text{O}_2$) show almost identical values compared to those of the $(\text{Zr})\text{BiVO}_4$ –NiFePB photoanode.

The above results explain a noticeably high photocatalytic activity for the system under study achieved by a simple deposition of an $\sim 10\text{--}15\text{ nm}$ thick NiFePB layer. In fact, this outstanding improvement can be attributed to many reasons. First, as initially pointed out by Aksoy et al. [38], the amorphous nature of the NiFePB shell has vital importance for the catalytic activity to be realized. As seen in the general formula of PB type polymers discussed above (see Scheme 1), the interstitial voids in the cyanide-bridged network are filled with alkali ions and/or zeolitic water. In a perfect FCC crystalline structure, both metals will be connected to either C or N atoms of the cyanide group, leaving no active sites except those on the surface. It is thus required to have reduced or no crystallinity at all in order to obtain a higher catalytic activity [38]. In the presence of suitable metal salt

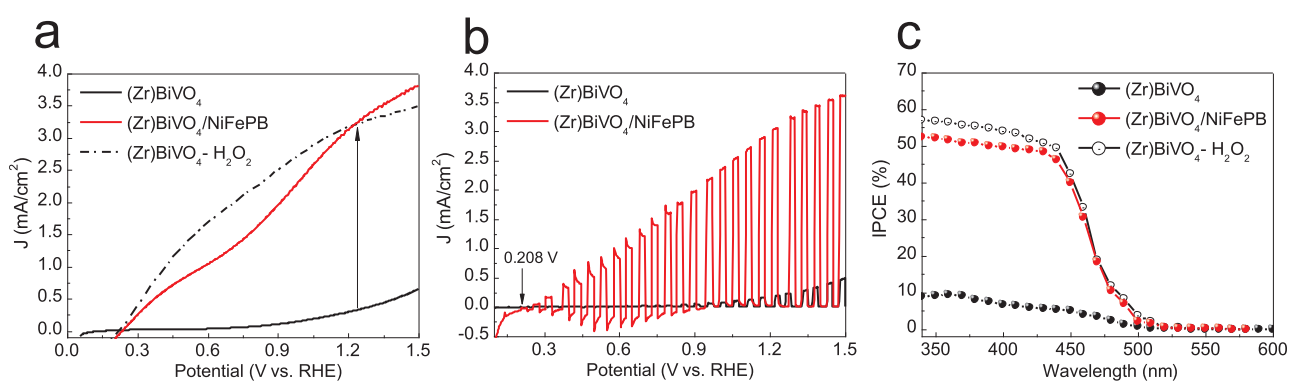


Fig. 3. (a) J–V curves of the $(\text{Zr})\text{BiVO}_4$ (black) and $(\text{Zr})\text{BiVO}_4$ –NiFePB (red) electrodes under continuous illumination of $100\text{ mW}\cdot\text{cm}^{-2}$. The black dashed J–V curve is carried on the $(\text{Zr})\text{BiVO}_4$ electrode with the addition $0.5\text{ M H}_2\text{O}_2$ as a hole scavenger. (b) J–V curves of the $(\text{Zr})\text{BiVO}_4$ (black) and $(\text{Zr})\text{BiVO}_4$ –NiFePB (red) electrodes under chopped illumination of $100\text{ mW}\cdot\text{cm}^{-2}$. (c) IPCE spectra for the $(\text{Zr})\text{BiVO}_4$ (black solid circles), $(\text{Zr})\text{BiVO}_4$ (black empty circles) with $0.5\text{ M H}_2\text{O}_2$ and $(\text{Zr})\text{BiVO}_4$ –NiFePB (red solid circles) electrodes.

precursors, Prussian blue materials usually undergo a rapid spontaneous precipitation that commonly hinders the control of crystallinity and composition [42]. Different methods have, however, been invented to improve such control [38,39,41,42]. In this work, our two-step process could successfully result in a purely amorphous NiFePB layer, explaining (at least partially) its high catalytic properties.

The second reason is the advantage delivered by our technique in providing the superior uniformity and conformity of the NiFePB coating coverage. Very recently, Hegner et al. reported BiVO_4 water oxidation photoanodes decorated with a CoFe-based PB material in which the BiVO_4 electrodes were sequentially immersed into CoCl_2 and $\text{K}_3[\text{Fe}(\text{CN})_6]$ solutions and the dipping times were optimized for both steps. Their procedure resulted in an amorphous CoFePB layer with a high current density of $\sim 1 \text{ mA}$ at 1.23 V vs. RHE and a noticeably low onset potential of 0.3 V [41]. The uniformity of CoFePB coverage was, however, inferior to what has been obtained in our work, for which the electrodeposition step of Ni is believed to be a crucial step. For comparison, $(\text{Zr})\text{BiVO}_4/\text{NiFePB}$ photoanodes were prepared by the sequential method adopted by Hegner et al., and the results are shown in Figures S14 and S15: decreased NiFePB coverage uniformity and less photocurrent enhancement are obtained.

The core-shell interfacial interaction in the $(\text{Zr})\text{BiVO}_4/\text{NiFePB}$ system was assessed by investigation of the charge transfer efficiencies (η_{CT}) and charge separation efficiencies (η_{CS}) at various applied potentials, and the results are presented in Fig. 4. Indeed, $(\text{Zr})\text{BiVO}_4$ photoanodes yield only $< 20\%$ η_{CT} (Fig. 4a), even at potentials as high as 1.23 V vs. RHE, at which the large electric field hinders surface recombination. After passivation with NiFePB, η_{CT} of the $(\text{Zr})\text{BiVO}_4/\text{NiFePB}$ composite photoanode is boosted to $\sim 90\%$ at 1.23 V vs. RHE, suggesting enhanced charge transfer kinetics. Similarly, η_{CS} of the $(\text{Zr})\text{BiVO}_4/\text{NiFePB}$ photoanode was evaluated to be 46.5% at 1.23 V vs. RHE, which represents a nearly two-fold enhancement in comparison to the uncoated $\text{Zr}(\text{BiVO}_4)$ photoanode (31.2% at 1.23 V vs. RHE). These results indicate that the NiFePB coating creates an efficient interface with water, which can be explained by the enormous number of available active sites promoted by the amorphous structure. The large

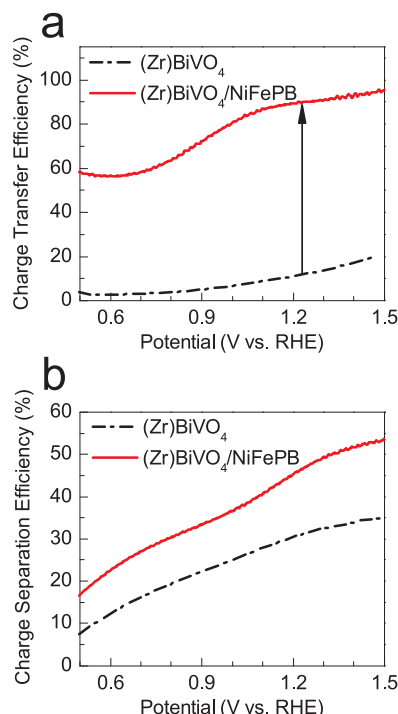


Fig. 4. Calculated (a) charge transfer efficiency (η_{CT}) and (b) charge separation efficiency (η_{CS}) as a function of applied potential for the $(\text{Zr})\text{BiVO}_4$ (black) and $(\text{Zr})\text{BiVO}_4/\text{NiFePB}$ (red) electrodes.

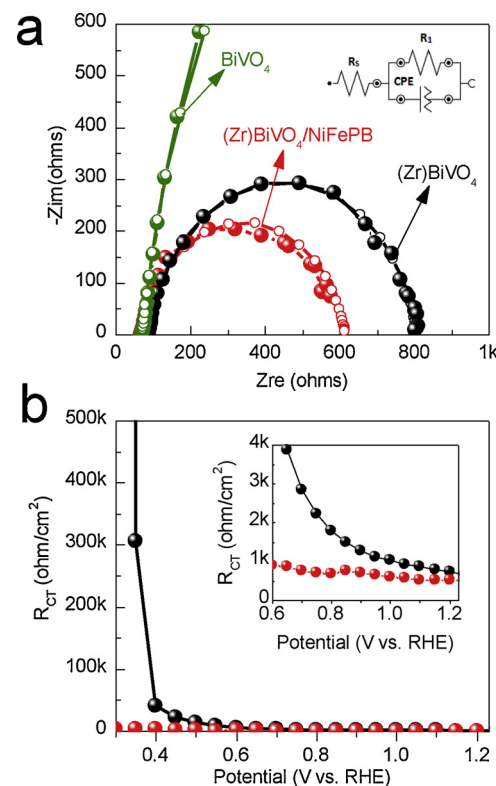


Fig. 5. (a) Nyquist plots under $100 \text{ mW} \cdot \text{cm}^{-2}$ illumination of bare BiVO_4 (green), $(\text{Zr})\text{BiVO}_4$ (black) and $(\text{Zr})\text{BiVO}_4/\text{NiFePB}$ (red) electrodes at 0.6 V with a frequency range between $100,000$ to 0.05 Hz . The solid circles represent the experimental data, while the open circles represent the data fitting to a simple Randles equivalent circuit, which is schematically drawn in the inset. (b) Calculated charge transfer resistance (R_{CT}) for $(\text{Zr})\text{BiVO}_4$ (black) and $(\text{Zr})\text{BiVO}_4/\text{NiFePB}$ (red) electrodes. The inset shows a magnified view of the high potential region of the same curve.

voids in the NiFePB framework also help to localize water molecules, also resulting in a more efficient charge transfer. NiFePB makes an energetically favorable interface with BiVO_4 as well, confirmed by the enhanced separation efficiency, which is also in agreement with previously published theoretical predictions [41,53].

The efficient charge transfer was also investigated by electrochemical impedance spectroscopy (EIS), as shown in Fig. 5. The Nyquist plots of the $(\text{Zr})\text{BiVO}_4/\text{NiFePB}$ photoanodes measured under illumination ($100 \text{ mW} \cdot \text{cm}^{-2}$) at 0.6 V vs. RHE and their corresponding equivalent circuit are shown in Fig. 5a. Evidently, the diameter of the arc radius on the EIS Nyquist plot of the $(\text{Zr})\text{BiVO}_4/\text{NiFePB}$ composite photoanode is much smaller than those of the BiVO_4 and $(\text{Zr})\text{BiVO}_4$ photoanodes, implying a faster interfacial charge transfer and more efficient separation of photogenerated charge carriers. At 0.6 V vs. RHE, the charge transfer resistance (R_{CT}) in the composite electrode is more than 4-fold lower than that of $(\text{Zr})\text{BiVO}_4$ (Fig. 5b).

The amount of evolved oxygen at the optimized $(\text{Zr})\text{BiVO}_4/\text{NiFePB}$ photoanode was monitored via oxygen fluorescence probe under an inert atmosphere. Fig. 6 shows the amount of evolved O_2 at 1.23 V vs. RHE after switching on the light source and associates it to the theoretical O_2 evolution (which assumes that all oxygen is produced by the generated photocurrent). The measured O_2 evolution is in agreement with the theoretically predicted values with a Faradaic efficiency of $\sim 90\%$.

3.3. Long-term stability

The long-term stability of the core/shell structured $(\text{Zr})\text{BiVO}_4/\text{NiFePB}$ photoanode was assessed by chronoamperometric

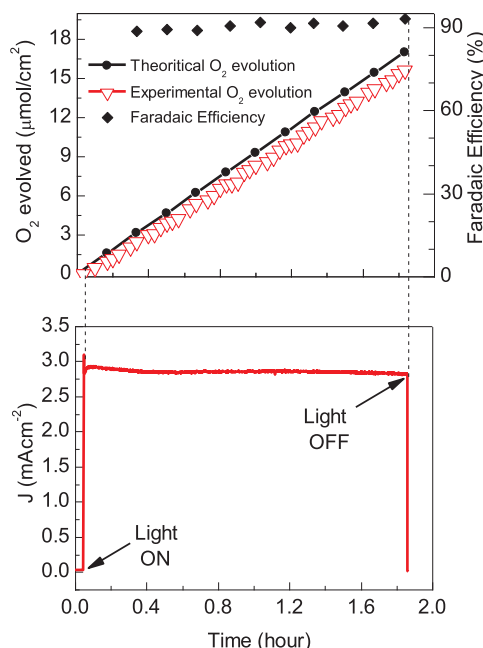


Fig. 6. Experimental (red triangles) and theoretical (black connected circles) as well as Faradaic efficiency (black rhombus) of (Zr)BiVO₄/NiFePB photoanode at 1.23 V vs RHE under 100 mWcm⁻² illumination. The current-time profile is simultaneously recorded and shown on the bottom curve.

measurements at 0.6 V vs. RHE in 0.1 M PBS (pH 7.5) under constant illumination of 100 mW.cm⁻², the results are shown in Fig. 7a. After an initial transient decrease of the photocurrent during the first 5 h, the photocurrent gradually increased, reaching ~ 70% of its original value in approximately 20 h. Surprisingly, when the light was switched off (for ~ 30 min) and on again, the photocurrent was completely retrieved followed by a slower rate of photocurrent decrease in the second on/off cycle, which eventually saturated at ~ 90% of the original value. We attribute this behavior, which was very reproducible for many fabricated samples, to photoinduced improvement of the (Zr)BiVO₄/NiFePB electrode that necessitates additional investigation. For example, PB type materials have been well-known for their photoinduced magnetization properties, which make them appealing for other applications like optical magnetic switching and molecule-based magnets [54–57]. The extent to which such phenomenon, and possibly others, is responsible for the observed transient light interaction effects needs further investigation. Nevertheless, the results definitely indicate highly stable electrodes with no material degradation over a time scale of ~ 60 h.

J-V measurements of the core-shell composite electrodes were additionally measured after the long-term stability testing, and the results are shown in Fig. 7b. The results evidence an increase in PEC performance in comparison with the fresh photoanode over a wide potential range which, as mentioned above, confirms the existence of a light-induced restorative effect. This makes Prussian blue materials more interesting and stimulates further possible investigations regarding their light interaction. UV-vis optical measurements before and after the J-t test are shown in Fig. 7c. Above the band edge (below ~ 460 nm), there is an ~ 20% decrease in the absorption signal that is compensated by the absorbance of newly created defects below the band edge. Although this indicates the creation of crystal defects in the BiVO₄ lattice (NiFePB is weakly absorbing in the UV-vis range), this result cannot stand for implying photocorrosion of any of the electrode materials. For further validation, the light-soaked electrode was examined by SEM and TEM measurements (Figure S4 and Figure S5), and no morphological changes or material deteriorations of the core-shell structure were observed. Indeed, the extent to which creation of defects

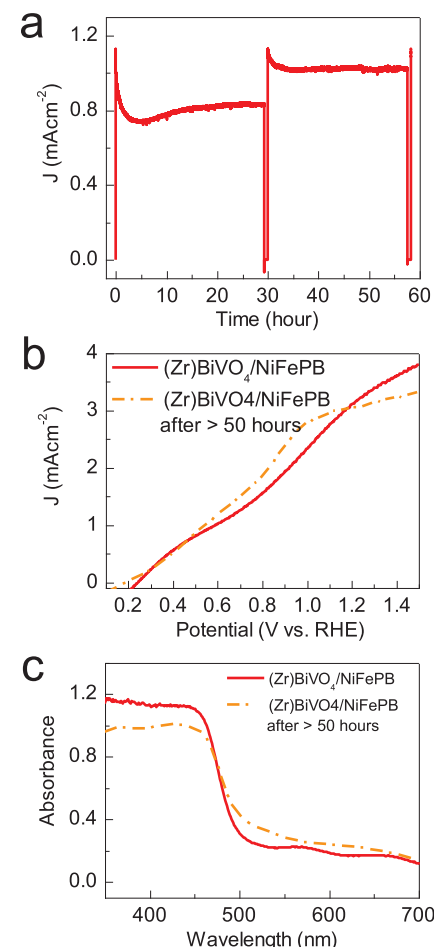


Fig. 7. (a) J-t curve for long-term photostability of (Zr)BiVO₄/NiFePB photoanode at 0.6 V vs. RHE for > 50 h under AM 1.5 G illumination. (b) J-V curves of (Zr)BiVO₄/NiFePB photoanode before (red) and after (orange) the J-t photostability test. (c) Absorbance of (Zr)BiVO₄/NiFePB photoanode before (red) and after (orange) the J-t test.

can affect the water oxidation process does not have a straightforward answer, and further investigations are still required.

The stability of the (Zr)BiVO₄ core was investigated by XRD measurements of the stability-tested (Zr)BiVO₄/NiFePB photoanode (Figure S6), and no degradation of the material crystallinity was observed. For the NiFePB shell, FT-IR measurement was carried out on the (Zr)BiVO₄/NiFePB photoanode after the long-term stability test (Figure S8). The vibrational band at 2095 cm⁻¹ showed no considerable decrease, indicating a stable NiFePB shell as well.

4. Conclusions

In summary, we developed a simple sequential method for creating (Zr)BiVO₄/NiFePB core/shell nanostructured photoanodes for photoelectrochemical water splitting. The method generates highly conformal NiFePB shell coating on the (Zr)BiVO₄ nanoparticles, which act as an efficient OECs on the (Zr)BiVO₄ surface. The (Zr)BiVO₄/NiFePB core-shell system resulted in a remarkable 10-fold increase of photocurrent (3.23 mAcm⁻² vs. RHE compared to 0.32 mAcm⁻² for the uncoated electrode) accompanied with a significantly low onset potential of 0.208 V vs. RHE and a long-term superior photostability tested for ~ 60 h. The amorphous nature of the coating in addition to its superior conformity are shown to be the key properties behind those improvements. Our work demonstrates the enormous potential of Prussian blue materials as efficient and robust OECs for BiVO₄.

electrodes and, possibly, for other semiconductors.

Conflicts of interest

There are no conflicts to declare.

Acknowledgement

The authors are grateful to the Deanship of Scientific Research, King Saud University for funding through Vice Deanship of Scientific Research Chairs.

Appendix A. Supplementary data

Supplementary material related to this article can be found, in the online version, at doi:<https://doi.org/10.1016/j.apcatb.2018.11.079>.

References

- [1] Wwf, the Energy Report 100% Renewable Energy by 2050, (2013).
- [2] M. Pagliaro, A.G. Konstandopoulos, R. Ciriminna, G. Palmisano, Solar hydrogen: fuel of the near future, *Energy Environ. Sci.* 3 (2010) 279.
- [3] M.G. Walter, E.L. Warren, J.R. McKone, S.W. Boettcher, Q. Mi, E.A. Santori, N.S. Lewis, Solar water splitting cells, *Chem. Rev.* 110 (2010) 6446–6473.
- [4] A. Fujishima, K. Honda, Electrochemical photolysis of water at a semiconductor electrode, *Nature* 238 (1972) 37–38.
- [5] P. Arunachalam, M.S. Amer, M.A. Ghanem, A.M. Al-Mayouf, D. Zhao, Activation effect of silver nanoparticles on the photoelectrochemical performance of mesoporous TiO_2 nanospheres photoanodes for water oxidation reaction, *Int. J. Hydrogen Energy* 42 (2017).
- [6] C. Du, X. Yang, M.T. Mayer, H. Hoyt, J. Xie, G. McMahon, G. Bischoping, D. Wang, Hematite-based water splitting with low turn-on voltages, *Angew. Chemie - Int. Ed.* 52 (2013) 12692–12695.
- [7] J.-W. Jang, C. Du, Y. Ye, Y. Lin, X. Yao, J. Thorne, E. Liu, G. McMahon, J. Zhu, A. Javey, J. Guo, D. Wang, Enabling unassisted solar water splitting by iron oxide and silicon, *Nat. Commun.* 6 (2015) 7447.
- [8] D.W. Hwang, J. Kim, T.J. Park, J.S. Lee, Mg-doped WO_3 as a novel photocatalyst for visible light-induced water splitting, *Catal. Letters* 80 (2002) 53–57.
- [9] X. Liu, F. Wang, Q. Wang, Nanostructure-based WO_3 photoanodes for photoelectrochemical water splitting, *Phys. Chem. Chem. Phys.* 14 (2012) 7894.
- [10] M. Sathish, B. Viswanathan, R.P. Viswanath, Alternate synthetic strategy for the preparation of CdS nanoparticles and its exploitation for water splitting, *Int. J. Hydrogen Energy* 31 (2006) 891–898.
- [11] Y. Xu, W. Zhao, R. Xu, Y. Shi, B. Zhang, Synthesis of ultrathin CdS nanosheets as efficient visible-light-driven water splitting photocatalysts for hydrogen evolution, *Chem. Commun.* 49 (2013) 9803.
- [12] Y. Park, K.J. McDonald, K.-S. Choi, Progress in bismuth vanadate photoanodes for use in solar water oxidation, *Chem. Soc. Rev.* 42 (2013) 2321–2337.
- [13] C. Martínez Suárez, S. Hernández, N. Russo, BiVO_4 as photocatalyst for solar fuels production through water splitting: a short review, *Appl. Catal. A Gen.* 504 (2015) 158–170.
- [14] Y. Liang, T. Tsubota, L.P.A. Mooij, R. Van De Krol, Highly improved quantum efficiencies for thin film BiVO_4 photoanodes, *J. Phys. Chem. C* 115 (2011) 17594–17598.
- [15] F.F. Abdi, N. Firet, R. vandeKrol, Efficient BiVO_4 thin film photoanodes modified with cobalt phosphate catalyst and W-doping, *ChemCatChem.* 5 (2013) 490–496.
- [16] J.A. Seabold, K. Zhu, N.R. Neale, Efficient solar photoelectrolysis by nanoporous Mo:BiVO_4 through controlled electron transport, *Phys. Chem. Chem. Phys.* 16 (2014) 11211–1131.
- [17] F.F. Abdi, T.J. Savenije, M.M. May, B. Dam, R. Van De Krol, The origin of slow carrier transport in BiVO_4 thin film photoanodes: A time-resolved microwave conductivity study, *J. Phys. Chem. Lett.* 4 (2013) 2752–2757.
- [18] M.N. Shaddad, M.A. Ghanem, A.M. Al-Mayouf, S. Gimenez, J. Bisquert, I. Herraiza-Cardona, Cooperative catalytic effect of ZrO_2 and $\text{alpha-Fe}_2\text{O}_3$ nanoparticles on BiVO_4 photoanodes for enhanced photoelectrochemical water splitting, *ChemSusChem.* 9 (2016) 2779–2783.
- [19] M.N. Shaddad, D. Cardenas-Morcoso, P. Arunachalam, M. Garcia-Tecedor, M.A. Ghanem, J. Bisquert, A. Al-Mayouf, S. Gimenez, Enhancing the optical absorption and interfacial properties of BiVO_4 with Ag_3PO_4 nanoparticles for efficient water splitting, *J. Phys. Chem. C.* (2018).
- [20] Y. Pihosh, I. Turkevych, K. Mawatari, T. Asai, T. Hisatomi, J. Uemura, M. Tosa, K. Shimamura, J. Kubota, K. Domen, T. Kitamori, Nanostructured $\text{WO}_3/\text{BiVO}_4$ photoanodes for efficient photoelectrochemical water splitting, *Small* 10 (2014) 1–8.
- [21] H. Ye, H.S. Park, A.J. Bard, Screening of electrocatalysts for photoelectrochemical water oxidation on W-doped BiVO_4 photocatalysts by scanning electrochemical microscopy, *J. Phys. Chem. C.* 115 (2011) 12464–12470.
- [22] D.K. Zhong, S. Choi, D.R. Gamelin, Near-complete suppression of surface recombination in solar photoelectrolysis by “co-Pi” catalyst-modified W:BiVO_4 , *J. Am. Chem. Soc.* 133 (2011) 18370–18377.
- [23] S.K. Pilli, T.E. Furtak, L.D. Brown, T.G. Deutsch, J.A. Turner, A.M. Herring, Cobalt-phosphate (Co-Pi) catalyst modified Mo-doped BiVO_4 photoelectrodes for solar water oxidation, *Energy Environ. Sci.* 4 (2011) 5028.
- [24] F.F. Abdi, R. Van De Krol, Nature and light dependence of bulk recombination in Co-Pi-catalyzed BiVO_4 photoanodes, *J. Phys. Chem. C.* 116 (2012) 9398–9404.
- [25] J.A. Seabold, K.S. Choi, Efficient and stable photo-oxidation of water by a bismuth vanadate photoanode coupled with an iron oxyhydroxide oxygen evolution catalyst, *J. Am. Chem. Soc.* 134 (2012) 2186–2192.
- [26] W.D. Chemelewski, H.C. Lee, J.F. Lin, A.J. Bard, C.B. Mullins, Amorphous FeOOH oxygen evolution reaction catalyst for photoelectrochemical water splitting, *J. Am. Chem. Soc.* 136 (2014) 2843–2850.
- [27] T.W. Kim, K.-S. Choi, Nanoporous BiVO_4 photoanodes with dual-layer oxygen evolution catalysts for solar water splitting, *Science* 343 (80) (2014) 990–994.
- [28] M. Zhong, T. Hisatomi, Y. Kuang, J. Zhao, M. Liu, A. Iwase, Q. Jia, H. Nishiyama, T. Minegishi, M. Nakabayashi, N. Shibata, R. Nishiro, C. Katayama, H. Shibano, M. Katayama, A. Kudo, T. Yamada, K. Domen, Surface modification of CoO_x loaded BiVO_4 photoanodes with ultrathin p-type NiO layers for improved solar water oxidation, *J. Am. Chem. Soc.* 137 (2015) 5053–5060.
- [29] D.K. Lee, K.-S. Choi, Enhancing long-term photostability of BiVO_4 photoanodes for solar water splitting by tuning electrolyte composition, *Nat. Energy.* (2017).
- [30] H.L. Tan, R. Amal, Y.H. Ng, Alternative strategies in improving the photocatalytic and photoelectrochemical activities of visible light-driven BiVO_4 : a review, *J. Mater. Chem. A Mater. Energy Sustain.* 5 (2017) 16498–16521.
- [31] A. Malathi, J. Madhavan, M. Ashokkumar, P. Arunachalam, A review on BiVO_4 photocatalyst: activity enhancement methods for solar photocatalytic applications, *Appl. Catal. A Gen.* 555 (2018) 47–74.
- [32] Y. Kuang, Q. Jia, G. Ma, T. Hisatomi, T. Minegishi, H. Nishiyama, M. Nakabayashi, N. Shibata, T. Yamada, A. Kudo, K. Domen, Ultrastable low-bias water splitting photoanodes via photocorrosion inhibition and in situ catalyst regeneration, *Nat. Energy* 2 (2017).
- [33] D. Bae, B. Seger, P.C.K. Vesborg, O. Hansen, I. Chorkendorff, Strategies for stable water splitting via protected photoelectrodes, *Chem. Soc. Rev.* 46 (2017) 1933–1954.
- [34] S. Pintado, S. Goberna-Ferrón, E.C. Escudero-Adán, J.R. Galán-Mascarós, Fast and persistent electrocatalytic water oxidation by Co-Fe Prussian blue coordination polymers, *J. Am. Chem. Soc.* 135 (2013) 13270–13273.
- [35] S. Goberna-Ferrón, W.Y. Hernández, B. Rodríguez-García, J.R. Galán-Mascarós, Light-driven water oxidation with metal hexacyanometallate heterogeneous catalysts, *ACS Catal.* 4 (2014) 1637–1641.
- [36] J.R. Galán-Mascarós, Water oxidation at electrodes modified with earth-abundant transition-metal catalysts, *ChemElectroChem.* 2 (2015) 37–50.
- [37] Y. Yamada, K. Oyama, R. Gates, S. Fukuzumi, High catalytic activity of heteropoly-nuclear cyanide complexes containing cobalt and platinum ions: visible-light driven water oxidation, *Angew. Chemie - Int. Ed.* 54 (2015) 5613–5617.
- [38] M. Aksoy, S.V.K. Nune, F. Karadas, A novel synthetic route for the preparation of an amorphous Co/Fe prussian blue coordination compound with high electrocatalytic water oxidation activity, *Inorg. Chem.* 55 (2016) 4301–4307.
- [39] H.T. Bui, N.K. Shrestha, S. Khadtare, C.D. Bathula, L. Giebel, Y.Y. Noh, S.H. Han, Anodically grown binder-free nickel hexacyanoferrate film: toward efficient water reduction and hexacyanoferrate film based full device for overall water splitting, *ACS Appl. Mater. Interfaces* 9 (2017) 18015–18021.
- [40] T. Shirakawa, M. Higashi, O. Tomita, R. Abe, Surface-modified metal sulfides as stable H_2 -evolving photocatalysts in Z-scheme water splitting with a $[\text{Fe}(\text{CN})_6]^{3-}/^{4-}$ redox mediator under visible-light irradiation, *Sustain. Energy Fuels.* 1 (2017) 1065–1073.
- [41] F.S. Hegner, I. Herraiza-Cardona, D. Cardenas-Morcoso, N. López, J.R. Galán-Mascarós, S. Gimenez, Cobalt hexacyanoferrate on BiVO_4 photoanodes for robust water splitting, *ACS Appl. Mater. Interfaces* 9 (2017) 37671–37681.
- [42] C.D. Wessells, S.V. Peddada, R.A. Huggins, Y. Cui, Nickel hexacyanoferrate nanoparticle electrodes for aqueous sodium and potassium ion batteries, *Nano Lett.* 11 (2011) 5421–5425.
- [43] Z. Yang, M. Xu, Y. Liu, F. He, F. Gao, Y. Su, H. Wei, Y. Zhang, Nitrogen-doped, carbon-rich, highly photoluminescent carbon dots from ammonium citrate, *Nanoscale* 6 (2014) 1890–1895.
- [44] J.M. Stillahn, K.J. Trevino, E.R. Fisher, Deposition of amorphous CN_x materials in BrCN plasmas: exploring adhesion behavior as an indicator of film properties, *ACS Appl. Mater. Interfaces* 3 (2011) 1402–1410.
- [45] Y. Feng, X.Y. Yu, Y. Paik, N-doped graphene layers encapsulated NiFe alloy nanoparticles derived from MOFs with superior electrochemical performance for oxygen evolution reaction, *Sci. Rep.* 6 (2016).
- [46] T.R.I. Cataldi, G.E. De Benedetto, A. Bianchini, X-ray photoelectron spectroscopic investigation and electrochemistry of polynuclear indium(III) hexacyanoferrate films, *J. Electroanal. Chem.* Lausanne (Lausanne) 448 (1998) 111–117.
- [47] K.B. Yatsimirskii, V.V. Nemoshkalenko, Y.P. Nazarenko, V.G. Aleshin, V.V. Zhilinskaya, N.A. Tomashevsky, Use of X-ray photoelectron and Mössbauer spectrometers in the study of iron pentacyanide complexes, *J. Electron Spectrosc. Relat. Phenomena* 10 (1977) 239–245.
- [48] H. Dotan, K. Sivula, M. Grätzel, A. Rothschild, S.C. Warren, Probing the photoelectrochemical properties of hematite ($\alpha\text{-Fe}_2\text{O}_3$) electrodes using hydrogen peroxide as a hole scavenger, *Energy Environ. Sci.* 4 (2011) 958.
- [49] F.F. Abdi, L. Han, A.H.M. Smets, M. Zeman, B. Dam, R. Van De Krol, Efficient solar water splitting by enhanced charge separation in a bismuth vanadate-silicon tandem photoelectrode, *Nat. Commun.* 4 (2013).
- [50] A.A. Karyakin, O.V. Gitelmacher, E.E. Karyakina, Prussian blue-based first-generation biosensor. A sensitive amperometric electrode for glucose, *Anal. Chem.* 67 (1995) 2419–2423.

[51] A.A. Karyakin, E.E. Karyakina, L. Gorton, Amperometric biosensor for glutamate using Prussian Blue-based “artificial peroxidase” as a transducer for hydrogen peroxide, *Anal. Chem.* 72 (2000) 1720–1723.

[52] A.A. Karyakin, E.A. Puganova, I.A. Budashov, I.N. Kurochkin, E.E. Karyakina, V.A. Levchenko, V.N. Matveyenko, S.D. Varfolomeyev, Prussian blue based nanoelectrode arrays for H_2O_2 detection, *Anal. Chem.* 76 (2004) 474–478.

[53] F.S. Hegner, D. Cardenas-Morcoso, S. Giménez, N. López, J.R. Galan-Mascaro, Level alignment as descriptor for Semiconductor/Catalyst systems in water splitting: the case of Hematite/Cobalt hexacyanoferrate photoanodes, *ChemSusChem.* 10 (2017) 4552–4560.

[54] A. Bleuzen, C. Lomenech, V. Escax, F. Villain, F. Varret, C. Cartier dit Moulin, M. Verdaguer, Photoinduced ferrimagnetic systems in Prussian blue analogues $C_x^{I}Co_4[Fe(CN)_6]_y$ (C^I = alkali cation). 1. Conditions to observe the phenomenon, *J. Am. Chem. Soc.* 122 (2000) 6648–6652.

[55] A. Goujon, O. Roubeau, F. Varret, A. Dolbecq, A. Bleuzen, M. Verdaguer, Photoexcitation from dia- to ferri-magnetism in a Rb-Co-hexacyanoferrate Prussian blue analogue, *Eur. Phys. J. B* 14 (2000) 115–124.

[56] Y. Arimoto, S. ichi Ohkoshi, Z.J. Zhong, H. Seino, Y. Mizobe, K. Hashimoto, Photoinduced magnetization in a two-dimensional cobalt octacyanotungstate, *J. Am. Chem. Soc.* 125 (2003) 9240–9241.

[57] A. Bordage, R. Moulin, E. Fonda, G. Fornasieri, E. Rivière, A. Bleuzen, Evidence of the Core-Shell Structure of (Photo)magnetic CoFe Prussian Blue Analogue Nanoparticles and Peculiar Behavior of the Surface Species, *J. Am. Chem. Soc.* 140 (2018) 10332–10343.